Earth and Planetary Science Letters 405 (2014) 142–155

Contents lists available at ScienceDirect

Earth and Planetary Science Letters

www.elsevier.com/locate/epsl

Anatomy of a megathrust: The 2010 M8.8 Maule, Chile earthquake rupture zone imaged using seismic tomography

Stephen P. Hicks [a,*], Andreas Rietbrock [a], Isabelle M.A. Ryder [a], Chao-Shing Lee [b], Matthew Miller [c]

[a] School of Environmental Sciences, University of Liverpool, Liverpool, Merseyside, L69 3GP, UK
[b] Institute of Applied Geosciences, National Taiwan Ocean University, Keelung, Taiwan
[c] Departamento de Geofísica, Universidad de Concepción, Concepción, Chile

ARTICLE INFO

Article history:
Received 25 May 2014
Received in revised form 19 August 2014
Accepted 26 August 2014
Available online 16 September 2014
Editor: P. Shearer

Keywords:
Maule earthquake
Chile
subduction
seismic zone
seismic tomography
OBS

ABSTRACT

Knowledge of seismic velocities in the seismogenic part of subduction zones can reveal how material properties may influence large ruptures. Observations of aftershocks that followed the 2010 M_w 8.8 Maule, Chile earthquake provide an exceptional dataset to examine the physical properties of a megathrust rupture zone. We manually analysed aftershocks from onshore seismic stations and ocean bottom seismometers to derive a 3-D velocity model of the rupture zone using local earthquake tomography. From the trench to the magmatic arc, our velocity model illuminates the main features within the subduction zone. We interpret an east-dipping high P-wave velocity anomaly (>6.9 km/s) as the subducting oceanic crust and a low P-wave velocity (<6.25 km/s) in the marine forearc as the accretionary complex. We find two large P-wave velocity anomalies (~7.8 km/s) beneath the coastline. These velocities indicate an ultramafic composition, possibly related to extension and a mantle upwelling during the Triassic.

We assess the role played by physical heterogeneity in governing megathrust behaviour. Greatest slip during the Maule earthquake occurred in areas of moderate P-wave velocity (6.5–7.5 km/s), where the interface is structurally more uniform. At shallow depths, high fluid pressure likely influenced the up-dip limit of seismic activity. The high velocity bodies lie above portions of the plate interface where there was reduced coseismic slip and minimal postseismic activity. The northern velocity anomaly may have acted as a structural discontinuity within the forearc, influencing the pronounced crustal seismicity in the Pichilemu region. Our work provides evidence for how the ancient geological structure of the forearc may influence the seismic behaviour of subduction megathrusts.

1. Introduction

Understanding the physical processes that control the behaviour of subduction zone megathrust faults remains one of earthquake seismology's main goals. The conceptual subduction zone asperity model (Lay and Kanamori, 1981) was developed to explain the inhomogeneous moment release of large earthquakes. Asperities are regions of the plate interface that produce the strongest slip, whereas barriers inhibit rupture. Roughness on the downgoing plate, such as seamounts can act as either asperities (e.g. Abercrombie et al., 2001) or barriers (e.g. Kodaira et al., 2004). Alternatively, features within the overriding plate, such as crustal batholiths (Sobiesiak et al., 2007), forearc basins (e.g. Song and Simons, 2003; Fuller et al., 2006) and faults (e.g. Audin et al., 2008) can also influence rupture behaviour. Based on the seismic characteristics of megathrust earthquakes, Lay et al. (2012) subdivide the subduction megathrust into five distinct depth domains. Knowledge of fault properties could reveal what governs this megathrust segmentation and the physical origins of asperities and barriers.

Seismic imaging methods can shed light on fault zone material properties. However, many subduction megathrusts lie offshore, where seismic instrumentation is deficient. This uneven station coverage reduces imaging capability and the mislocation of offshore earthquakes. With its coastline lying <100 km to the trench in places, the Central Chile margin (Fig. 1), is an ideal natural laboratory to study the subduction interface.

In 2010, an M_w 8.8 earthquake struck the Maule region of Central Chile. Following the earthquake, a dense seismometer network was deployed on the forearc to record aftershocks (e.g. Rietbrock et al., 2012). Fortunately, this onshore network was supplemented by ocean-bottom seismometer (OBS) deployments, dramatically improving station coverage (Fig. 2). Studies of preseismic locking (e.g. Moreno et al., 2010), the coseismic rupture (e.g.

* Corresponding author.

http://dx.doi.org/10.1016/j.epsl.2014.08.028

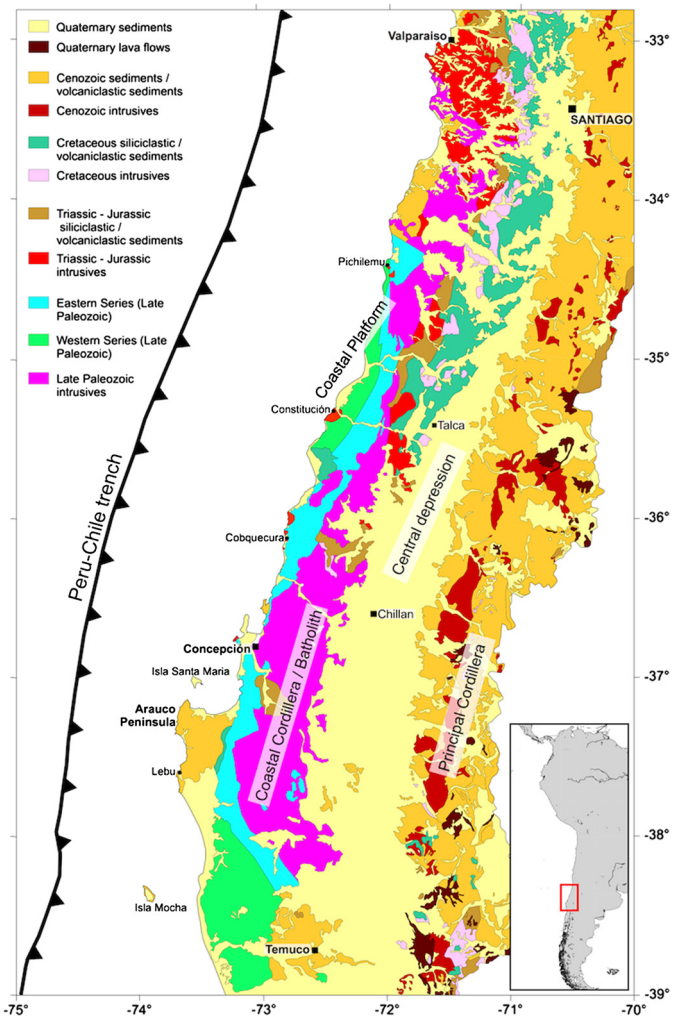

Fig. 1. Geotectonic characteristics and simplified geological map of the South Central Chilean margin. Morphotectonic units from Glodny et al. (2007) and geological map redrawn after SERNAGEOMIN (2003), Melnick and Echtler (2006) and Vásquez et al. (2011). The red box in the inset map gives the location of the study area. Labels show the names of the locations referred to in this paper. (For interpretation of the references to colour in this figure legend, the reader is referred to the web version of this article.)

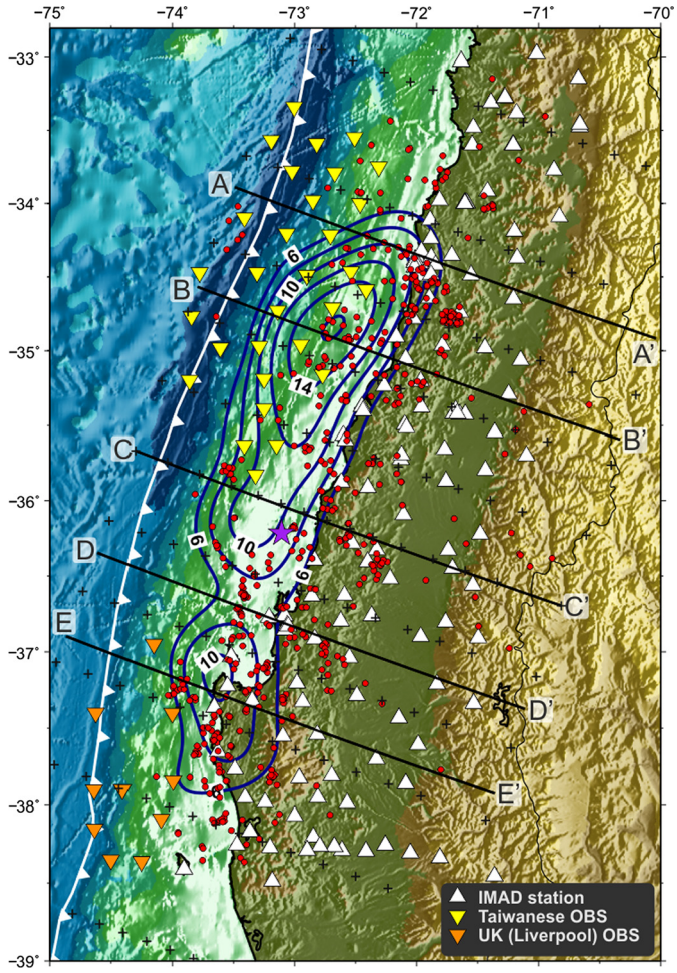

Fig. 2. Map of the Maule segment along the South Central Chile margin coloured by bathymetry/topography. The main rupture characteristics of the Maule earthquake are shown. The purple star shows the rupture's epicentre (Hayes et al., 2013) and the blue contours represent coseismic slip distribution (>6 m) in 2 m intervals (Moreno et al., 2012). Triangles correspond to seismic stations used in the velocity inversions. Black crosses indicate the horizontal grid nodes used in the 3-D inversion and red circles show preliminary locations of the 669 earthquakes used in the velocity inversions. Thick black lines show the location of cross-sections that are shown in this paper. (For interpretation of the references to colour in this figure legend, the reader is referred to the web version of this article.)

Moreno et al., 2012) and postseismic deformation (e.g. Lin et al., 2013) describe the behaviour of the Maule megathrust at different stages of the seismic cycle. This behaviour suggests that spatial variations in physical properties could exist in the fault zone.

The purpose of our study is to detect physical heterogeneity along the Maule megathrust using seismic tomography. In a preliminary tomographic study of the rupture zone based on automatically-determined P- and S-wave arrival times from early aftershocks, Hicks et al. (2012) identified a large seismic velocity anomaly lying along the plate interface. This previous study, however, used only observations from onshore stations, resulting in reduced offshore imaging capability. To build on this work, we have manually analysed aftershock data and incorporated OBS stations to derive a detailed three-dimensional (3-D) velocity model of the rupture zone. We examine the quality of our velocity model by analysing the resolution matrix and by testing characteristic models. We compare fault velocity structure with behaviour during the seismic cycle, providing valuable insight into the physical origins of asperities and barriers.

2. Characteristics of the Central Chile subduction zone

Along the Central Chilean margin, earthquakes are driven by subduction of the Nazca plate beneath the South American plate at a rate of 74 mm/yr (e.g. DeMets et al., 2010). Large earthquake ruptures along the margin tend to occur within highly coupled segments (Métois et al., 2012). We focus on the Maule segment, which is demarcated by the Mocha Block to the south and the Juan Fernández Ridge to the north (Contreras-Reyes et al., 2013). The Maule segment last fully ruptured during the great 1835 Concepción earthquake and was recognised as a mature seismic gap (e.g. Ruegg et al., 2009).

Active- and passive-source seismic studies have established the deep subsurface structure in parts of the Maule segment. The 7 km thick oceanic crust subducts at an angle of ~6° beneath the trench (Contreras Reyes et al., 2008; Moscoso et al., 2011), steepening to ~15° beneath the coastline (e.g. Haberland et al., 2009; Hayes et al., 2012). The marine forearc comprises two domains: the frontal accretionary prism and the paleo-accretionary complex (outer wedge) (e.g. Contreras Reyes et al., 2008). The continental Moho intersects the subducting plate beneath the eastern

coastal ranges; however, its exact position is debated. Based on local earthquake tomography, Hicks et al. (2012) place the slab-mantle intersection at ~50 km depth, similar to that estimated south of the Maule segment (e.g. Haberland et al., 2009). Conversely, Dannowski et al. (2013) postulate that based on receiver functions, the intersection lies at ~38 km depth in the Maule segment. Further east, the continental crust thins to ~30 km, defining the underlying arch-shaped, high velocity continental mantle (e.g. Haberland et al., 2009). Hicks et al. (2012) describe a high P-wave velocity anomaly on the plate interface beneath the coastal cordillera at 36°S that was interpreted as a subducted seamount.

The geology of the coastal cordillera (Fig. 1) encompasses a late-Paleozoic paired intrusive-metamorphic belt with two series of metasediments (e.g. Martin et al., 1999). The Western Series constitutes low-grade metapsammopelitic rocks with intercalations of metabasite derived from an ancient accretionary prism. Along the eastern coastal cordillera, late Paleozoic granite batholiths intrude the Eastern Series. The composition of these granites indicates a shallow, crustal-derived source (Lucassen et al., 2004). Although these Paleozoic rocks dominate the surface geology, outcrops of Triassic plutons lie along the coastline. Some of these intrusions contain fayalite, indicating a mantle-derived magmatic source (Vásquez and Franz, 2008). The intrusions were emplaced when the margin was undergoing post-orogenic collapse and rifting, marking the transitional period between Gondwanan amalgamation and contemporary Andean-style subduction (Vásquez et al., 2011).

3. The 2010 Maule earthquake

On February 27, 2010, an M_w 8.8 earthquake ruptured a ~500 km long portion of the Maule segment. The earthquake nucleated offshore, 25 km from the coastline (Fig. 2) (Hayes et al., 2013). Coseismic slip models for the rupture show that most slip occurred between the trench and the coastline. The models further reveal that two asperities were ruptured during the earthquake: one to the north, the other to the south of the mainshock epicentre (Fig. 2). In this paper, we refer to the coseismic slip models of Moreno et al. (2012) and Lin et al. (2013) since these use the most complete datasets. Teleseismic back-projection reveals that high frequency radiation came from a deeper part of the fault, of which the overall pattern suggests triggering on distinct portions of megathrust (Kiser and Ishii, 2011).

Following the rupture, most aftershocks occurred along the plate interface at 10–35 km depth, with a second band at 40–45 km depth (Lange et al., 2012; Rietbrock et al., 2012). Hicks et al. (2012) showed that the resulting gap in seismicity coincides with the location of a high P-wave velocity anomaly. Another feature of the aftershock sequence was intense shallow, normal faulting seismicity in the north, near Pichilemu (e.g. Ryder et al., 2012). Bedford et al. (2013) and Lin et al. (2013) indicate that most postseismic deformation was aseismically released, assumed to be afterslip. Bedford et al. (2013) show that most afterslip occurred seaward of the coastline; Lin et al. (2013) suggest most afterslip occurred landward of the coastline.

4. Seismic data

4.1. Temporary seismic networks

Following the Maule earthquake, teams from Chile, the US and Europe installed seismometers in the rupture area to record aftershock seismicity. The International Maule Aftershock Deployment (IMAD) comprised ~160 three-component broadband instruments on the continental forearc (Fig. 2). Most stations were deployed within one month after the earthquake. Station coverage peaked between April and June 2010, with many stations active until September 2010. Onshore data alone, however, is insufficient for accurately imaging the offshore region, where most coseismic and aftershock activity occurred.

Fortunately, following the Maule earthquake, UK and Taiwanese institutions deployed two separate OBS networks in the rupture area (Fig. 2). The Taiwanese deployment comprised 17 OBS that were initially active from 15th July to 8th August 2010. The stations were then moved northward in a second stage from 14th August to 6th September. The UK deployment had 10 OBS instruments offshore of the Arauco Peninsula from August 2010 to March 2011.

4.2. Catalogue selection, travel-time picks and initial event locations

For a well-resolved tomography model, we require a uniform source–receiver distribution across the rupture area to ensure that resolving capability is even across the model. Due to the uneven aftershock distribution, we used a set of criteria to select the event dataset. From an automatic catalogue (Rietbrock et al., 2012), we first chose events with large magnitudes ($M_l > 4$) so that many clear onsets are recorded throughout the network. Second, we subdivided the area into smaller 2500 km^2 blocks and selected an equal number of events in each, ensuring an even event distribution. Third, we selected events that were located within each OBS network during their operational periods. Fortunately, both the northern and southern OBS networks were simultaneously active for 15 days (22/08/10–06/09/10); therefore, as a final step, we chose events located between these two networks during this time window.

The above criteria resulted in an initial catalogue of 710 events. We manually determined onset times of P- and S-waves for these events using the SDX software (http://doree.esc.liv.ac.uk:8080/sdx). Based on onset time uncertainties, we assigned each observation a weight as follows: Weight 0 (<0.04 s); Weight 1 (0.04–0.1 s); Weight 2 (0.1–0.2 s); Weight 3 (0.2–1 s); Weight 4 (>1 s). Using these onset times, we located the events inside the one-dimensional (1-D) velocity model of Haberland et al. (2006) using HYPO71PC (Lee and Valdes, 1985). We rejected events with an azimuthal GAP >270° and with fewer than 12 P-wave and 4 S-wave observations. We also rejected all observations with weights of 3 and 4. Applying these criteria reduced the initial dataset by 6%, leaving a high-quality catalogue of 669 events (Fig. 2) with 38,000 P-wave and 13,000 S-wave onset times.

5. Velocity inversion strategy

We used a staggered velocity inversion scheme (e.g. Haberland et al., 2009; Collings et al., 2012) in which we inverted for 1-D model, followed by a coarse 2-D model, a fine 2-D model, and finally a 3-D model. Such a strategy ensures that a smooth regional velocity model in the trench-perpendicular direction can be established without leaving velocity artefacts (from the 1-D model) in poorly resolved regions, which may affect event locations. Establishing a 2-D model with robust earthquake locations is therefore an important step before resolving any 3-D (trench-parallel) velocity variations. At each step, we chose damping values from trade-off curves of data variance versus model complexity (e.g. Eberhart Phillips, 1986). The inversion parameters at each stage are summarised in Table S1.

5.1. 1-D inversion

We selected events located inside the network (GAP < 180°), leaving 627 events for the 1-D inversion. We inverted for P-wave velocity (v_p) and S-wave velocity (v_s) using VELEST (Kissling et al.,

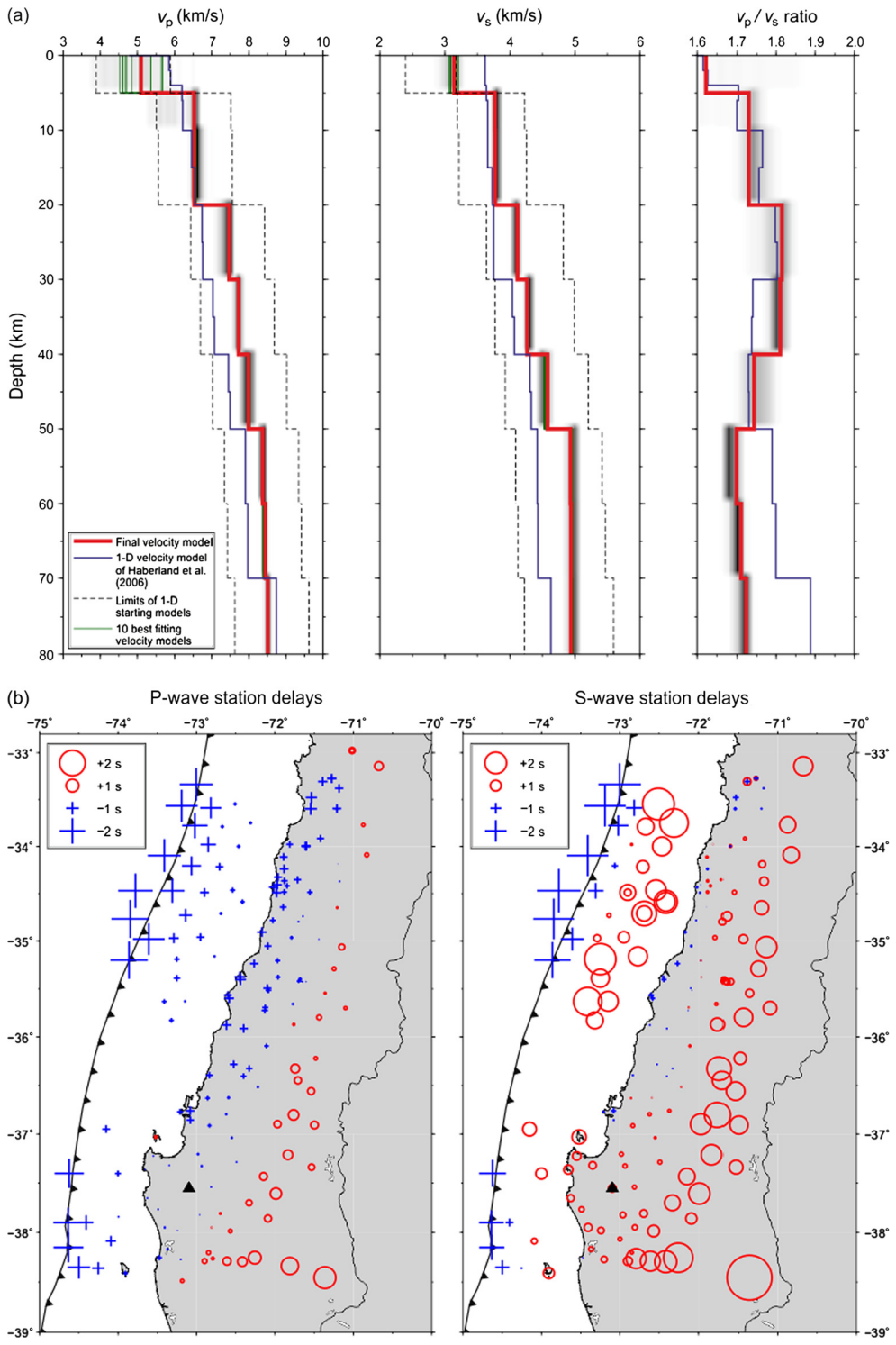

Fig. 3. Results of the 1-D velocity model inversion. (a) 1-D velocity models showing the range of starting models, range of inverted models (grey shading), and the final velocity model. (b) Map of 1-D station delay terms. The reference station is indicated by the black triangle.

1994). VELEST requires that all stations are located within the uppermost layer. However, the greatest station elevation is 2.2 km and deepest OBS station lies 5.4 km below sea level; a model with an 8 km thick uppermost layer is impractical. We negated this problem by following the strategy of Husen et al. (1999), setting station elevations to zero and allowing station terms to absorb systematic travel-time errors. We kept station damping low in the 1-D inversion to ensure that station terms accounted for station elevations and regional 2-D velocity variations. For the 1-D inversion, we tested 2000 initial models that were generated by randomly perturbing the velocity of each layer in our starting model (Haberland et al., 2006). In each inversion, we used a v_p/v_s ratio of 1.79, as determined from Wadati diagram analysis. From the 2000 inversions, we selected the model with the lowest RMS residual as our best v_p model and then inverted for a 1-D v_s model.

The best-fitting 1-D model (Fig. 3a) has low v_p of 5.1 km/s at shallow depths, increasing to 6.1 km/s at 5 km depth. Velocities of greater than 7 km/s are reached at 20 km depth. The uppermost

layer of the minimum 1-D model is poorly constrained due to the lack of shallow events and expected velocity structure differences between the offshore and onshore areas. Velocities in the uppermost layer are ~0.8 km/s slower than the model of Haberland et al. (2006), a result of the greater quantity of offshore observations in our study.

Station delays are important for generating accurate 1-D event locations if the subsurface has significant 2-D velocity variations. We find large negative delays for both P-waves (>−3.0 s) and S-waves (>−2.7 s) at OBS stations located offshore of the trench axis (Fig. 3b). The P-wave station terms increase toward the magmatic arc, with stations here having the largest P-wave delays (<1.7 s). There is also a trench-parallel variation in onshore P-wave station terms, with values more positive in the south. In contrast, S-wave delays are large and positive at stations on the continental shelf (up to 2.9 s). The systematic trench-perpendicular variation in station delays mainly results from dipping structures in the subsurface, and to a lesser extent from station elevation differences.

5.2. 2-D and 3-D tomographic inversion

For the 2-D and 3-D tomographic inversions, we used SIMUL2000 (Thurber, 1983; Eberhart Phillips and Michael, 1998). This algorithm simultaneously inverts for seismic velocity and hypocentral parameters using an iterative damped least squares method; it uses a direct inversion for v_p/v_s ratio to account for the reduced number of high-quality S-wave observations compared to P-wave observations. Velocities are inverted on a rectangular grid of nodes with linear B-spline interpolation. In each inversion, we did not invert for station corrections and kept hypocentres fixed for the first three iterations.

We first inverted for a coarse 2-D model, in which a 3-D grid was used, but velocity nodes in the along-strike direction were kept fixed, effectively forming a 2-D inversion. The 2-D inversion grid had a uniform horizontal grid spacing of 25 km and 10 km spacing in depth. Beneath the outer rise and trench, we linked vertically adjacent nodes at depths of 15 km or greater due to the diminished ray coverage. Linking nodes (Thurber and Eberhart Phillips, 1999) allows for coarser node spacing in parts of the model. Without linking nodes, we found that the inversion introduced low velocity artefacts in this part of the model, biasing earthquake depths beneath the outer rise. For the fine 2-D and 3-D inversions, we used a minimum horizontal grid spacing of 16 km and a minimum vertical spacing of 8 km. For the 3-D inversion, we introduced a set of nodes in the trench-parallel direction, each 55 km apart, providing 13 nodes to image velocity variations in the trench-parallel direction (Fig. 2). This nodal spacing allows for a finer resolution image than that achieved by Hicks et al. (2012).

For the coarse 2-D inversion, we used events inside the network (GAP < 180°) to establish the main velocity structure. Nonetheless, a test showed that when the closest stations were located more than 40 km from an earthquake, its depth was poorly constrained. This finding was important for events located in between the two OBS networks (Chen et al., 1982; Frohlich et al., 1982). Therefore, we only chose events that had the closest two stations at an epicentral distance of less than 40 km. These criteria resulted in a catalogue of 589 events for the coarse 2-D inversion. Once the main velocity structure was established, we subsequently relaxed the GAP criterion to 210° for the fine 2-D inversion to improve ray coverage at the edges.

Finally, to improve the lateral imaging capability of our inversions, we applied an extra smoothing technique. We performed two additional inversions, each shifting the horizontal node locations by a third of the nodal spacing, and calculating the average velocity of these. For the 3-D inversion, we also performed this averaging in the trench-parallel direction. Such an averaging technique has been used in local earthquake tomography studies (e.g. Haberland et al., 2009; Collings et al., 2012).

6. Inversion resolution

6.1. Resolution tests

Our first resolution test focussed on the full model resolution matrix (MRM). Nodes with good ray coverage have large diagonal elements of the MRM; nodes with poor coverage have small diagonal elements of the MRM due to their dependency on adjacent grid points. This effect is known as smearing. We estimated the magnitude of smearing by calculating the spread function (Toomey and Foulger, 1989), which assesses the ratio between off-diagonal and diagonal terms. To accurately visualise the direction and size of smearing of nodes, we contoured each row of the MRM at the 70% value of its corresponding diagonal element.

As another resolution test, we analysed the sensitivity of our velocity models to the event catalogue; we achieved this by performing a bootstrap resampling. Compared to formal MRM analysis, bootstrap resampling is useful because noise is intrinsically contained within the dataset. Calvert et al. (2000) suggest that such event-based resampling should produce similar results to resampling individual picks. We randomly resampled the event catalogue, forming a catalogue of 530 events (80% of our original catalogue). Once the 530 events were chosen, we randomly chose duplicate events, ensuring the catalogue was of the same size as for the actual inversion (589 events). Using the same inversion workflow, the velocity models were then stored and the process repeated 100 times.

As a final assessment of imaging capability, we carried out restoring resolution tests. By designing synthetic velocity models, we assessed the capacity of our dataset to resolve the geometry and amplitude of velocity anomalies. We calculated synthetic travel times using the true source–receiver geometry. To reflect the true quality of our observations, Gaussian noise was added to the travel times with a standard deviation depending on onset time uncertainties (0.04–0.2 s). We then inverted the travel-times using the same workflow as per our real inversion. We designed the synthetic velocity model with two objectives in mind. First, we examined whether our inversion could constrain the geometry and amplitude of high velocity bodies lying along the plate interface that were identified by Hicks et al. (2012). Second, we tested whether we could resolve lateral variations of v_p/v_s ratio in the subducting oceanic crust. Our input model also comprised the main domains of the Central Chile subduction zone identified in previous studies (e.g. Haberland et al., 2009). The final 3-D model used as input for the restoring resolution test is shown in Fig. 4 (v_p) and Fig. S3 (v_p/v_s).

6.2. 2-D model resolution

MRM analysis of the 2-D v_p model (Fig. S1) shows that most nodes have large diagonal elements and symmetric resolution kernels. This finding indicates that in most parts, the model is well resolved up to the trench and to depths of 80–90 km beneath the Central Depression. Compared with the tomographic model of Hicks et al. (2012) for the Maule region, the inclusion of OBS data dramatically improves imaging resolution of the marine forearc. Beneath the magmatic arc, at depths of 20–90 km, diagonal elements are small with large and elongate resolution contours, indicating poor resolution. Resolution is also poor west of the trench, beneath the outer rise. From the results of the bootstrapped event resampling (Fig. S2), v_p is well constrained throughout the model ($\sigma < 0.01$ km/s), indicating that the model is insensitive to the event selection criteria. Overall, the continental forearc (10–40 km

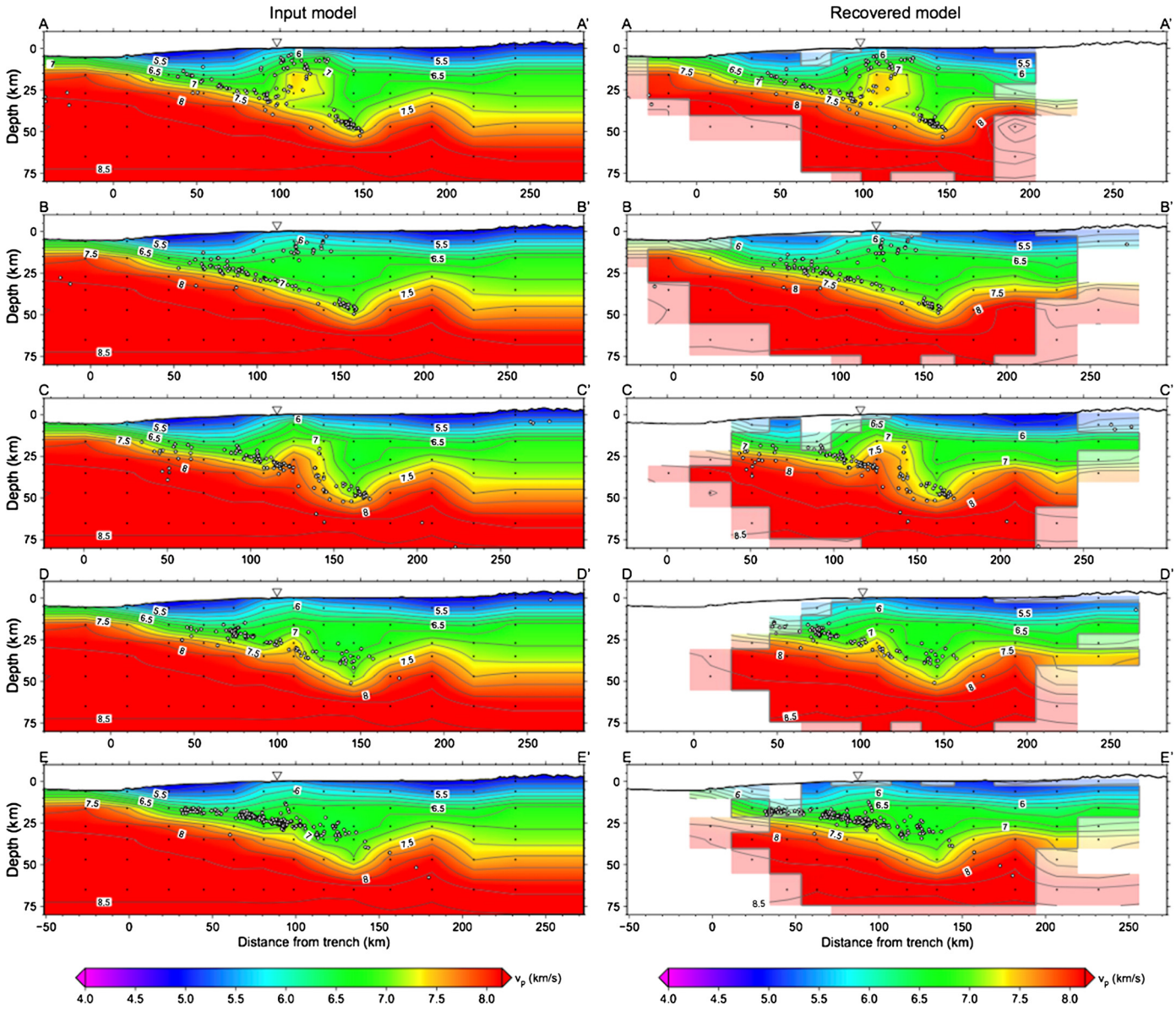

Fig. 4. (left) Synthetic 3-D v_p input model and (right) corresponding inversion results for the restoring resolution test. Locations of the five cross-sections are shown in Fig. 2. Black crosses indicate the location of inversion nodes and white dots indicate the locations of the 669 earthquakes used. Regions of the model with good resolution are bounded by the thick grey line. Regions with reduced resolution are faded; regions with no resolution are left blank. The location of the coastline is denoted by the white triangle.

depth) is the best-resolved part of the 2-D v_p model. The resolution tests indicate that the size of resolved features varies with depth due to the irregular source–receiver distribution. For example, we are unable to sufficiently resolve a thin low-velocity structure at 50–80 km depth (Fig. S4), such as that imaged at the base of the continental mantle by Haberland et al. (2009). This poor resolution at greater depths is due to the lack of intermediate depth aftershocks beneath the Central Depression and magmatic arc (Fig. 2).

For the 2-D v_p/v_s ratio model, spread values are higher and resolution kernels are larger than in the v_p model. This is likely due to our dataset comprising 66% fewer S-wave than P-wave observations, and fewer S observations at larger epicentral distances. Some vertical smearing is present at shallow and deep nodes beneath the marine forearc, but overall, the well-resolved areas are comparable to that of the v_p model. The maximum σ for v_p/v_s is 0.04.

Based on the combined interpretation of the results from our resolution tests, spread values of less than 2.1 and 4.2 represent well-resolved areas in the 2-D v_p and v_p/v_s ratio models, respectively. Laterally, we are able to resolve the subducting oceanic lithosphere from the trench to ~80 km depth beneath the magmatic arc. Both the marine and continental forearcs are well resolved.

6.3. 3-D model resolution

From the restoring resolution tests (Fig. 4), the 3-D inversion is able to accurately recover the shape and amplitude of the input anomalies. In the continental mantle, v_p is overestimated by ~13% and velocities in the shallow marine forearc are ~30% too fast. Amplitudes of high velocity anomalies in the subducting crust are well recovered. Likewise, for v_p/v_s ratio, the inversion is able to recover most features of the input model, but is not able to fully recover patches of high v_p/v_s ratio in the subducting lithosphere

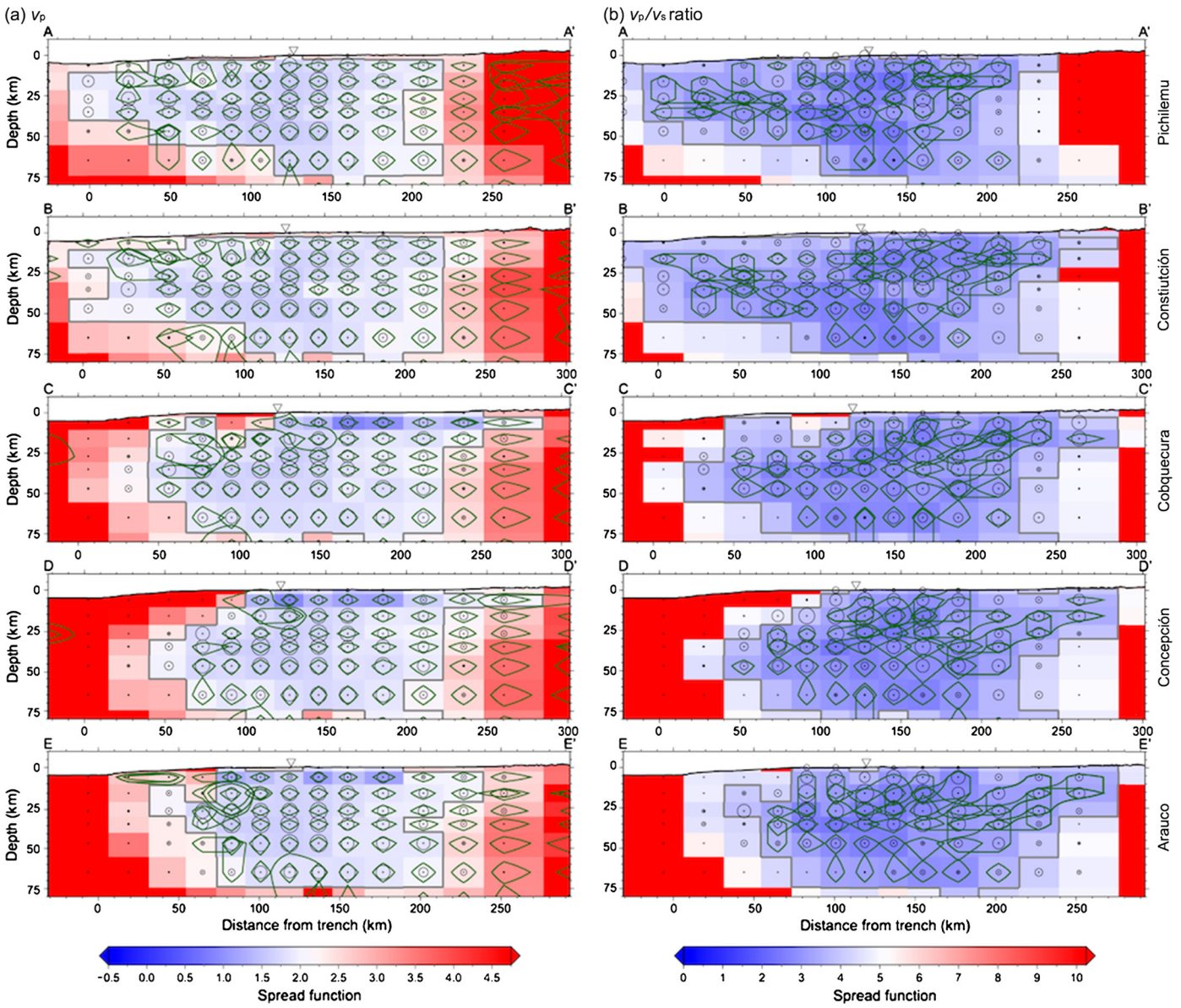

Fig. 5. Resolution estimate of our 3-D velocity model based on analysis of the model resolution matrix. At each node, the different colours indicate spread function values, black circles represent diagonal elements of the resolution matrix and green lines correspond to the 70% contour of the resolution kernel. Locations of the five cross-sections are shown in Fig. 2. Black crosses indicate the location of inversion nodes. Regions of the model with good resolution are bounded by the thick grey line. The location of the coastline is denoted by the white triangle. (For interpretation of the references to colour in this figure legend, the reader is referred to the web version of this article.)

(Fig. S3). In the Central Depression, shallow marine forearc and continental mantle, v_p/v_s values are exaggerated by around 2%.

MRM analysis of the 3-D model (Fig. 5) shows that the well-resolved area in each cross-section is broadly similar to that of the 2-D v_p model. Nodes in the southernmost cross-section have strong smearing beneath the magmatic arc. The offshore region is poorly resolved at ~36°S due to the lack of OBS coverage here. In the north, however, nodes are well resolved up to the trench because of the denser OBS coverage. Along the onshore forearc, resolution is best in the north due to abundant crustal seismicity. Although its resolution is lower, the v_p/v_s ratio anomalies are real (as shown by the restoring resolution test) but anomalies could be averaged over a distance greater than the node spacing (Eberhart Phillips et al., 2005). Overall, spread values of less than 2.1 indicate good resolution in the 3-D v_p model. The resolving capability of the 3-D v_p/v_s ratio model is broadly similar to that of the v_p model, with spread values of less than 4.1 indicating good resolution.

7. Results and discussion

7.1. Description and interpretation of velocity models

The 2-D and 3-D models show the regional first-order velocity structure previously observed for the Central Chilean margin (e.g. Haberland et al., 2009). The 2-D model is shown on a cross-section in Fig. 6. The 3-D model is displayed on vertical and horizontal sections in Fig. 7 and Fig. 8, respectively. Features described in this section correspond to labels in the figures.

7.1.1. Subducting oceanic lithosphere

The most prominent feature of the velocity models is an east-dipping structure with high v_p (6.9–8 km/s), (labelled '*oc*'). This feature also has a strong v_p gradient and elevated v_p/v_s ratio of 1.80–1.85 (Poisson's ratio of 0.28–0.29) along the main band of seismicity. These velocities are in agreement with previous studies in the area (e.g. Contreras Reyes et al., 2008; Haberland et al.,

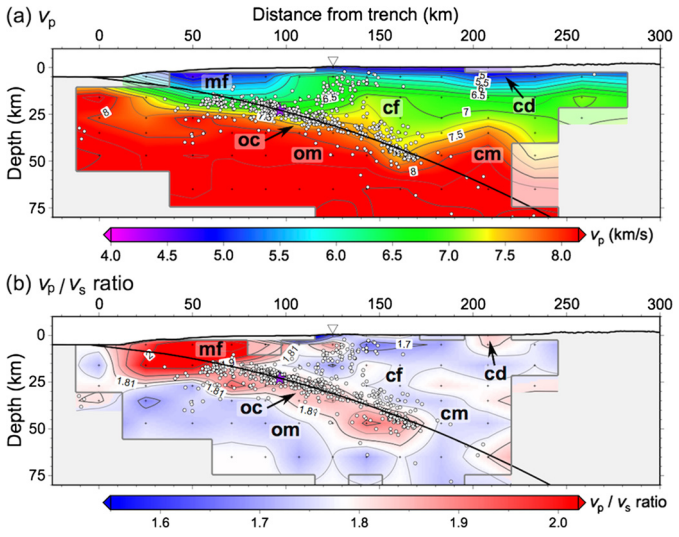

Fig. 6. 2-D velocity model plotted on a cross-section oriented perpendicular to the trench. Crosses indicate grid nodes and white circles give the 2-D locations of events from the tomographic inversion. Based on analysis of the MRM and the characteristic model tests, limits of well-resolved areas are given by the thick grey line. Regions with diminished resolution are faded; unresolved regions are left blank. Labels refer to the following features that are discussed in the text: mf = marine forearc; oc = oceanic crust; cf = upper forearc crust; cd = Central Depression; cm = continental mantle. The thick black line indicates the location of our calculated plate interface. The purple star denotes the hypocentral location of the Maule earthquake (Hayes et al., 2013). The location of the coastline is denoted by the white triangle. (For interpretation of the references to colour in this figure legend, the reader is referred to the web version of this article.)

2009) and indicative of either hydrated oceanic crustal material (e.g. Hacker and Abers, 2004) or high pore fluid pressure. Based on velocity contours alone and the high v_p/v_s ratio anomaly, we are unable to trace the oceanic lithosphere to depths of more than 50 km, indicating that the crust has a lower pore pressure or is less hydrated at these depths. From our tomographic images, we are unable to determine the exact location of the oceanic Moho. Assuming a 7 km thick crust (e.g. Contreras Reyes et al., 2008), the mid-lower oceanic mantle has v_p of 7.8–8.5 km/s and a low v_p/v_s ratio (1.70–1.76) (Poisson's ratio of 0.24–0.26), suggesting it is not hydrated.

7.1.2. Marine forearc

The offshore forearc region (labelled '*mf*') comprises low v_p (4.75–6.25 km/s) and a high v_p/v_s ratio of (1.9–2.2). The location of such velocities is consistent with sediments and meta-sediments in the frontal prism and outer wedge, respectively. These v_p/v_s ratios correspond to a Poisson's ratio of 0.31–0.37. Tsuji et al. (2008) relate such values to overpressured sediments in a pore pressure model for the Nankai accretionary prism. Beneath the coastline, a strong horizontal v_p gradient represents the boundary between the outer wedge and the upper continental forearc. Studies find similar velocities in the marine forearc south of the Maule segment (Contreras Reyes et al., 2008; Haberland et al., 2009) and in other subduction zones (Reyners et al., 2006; Collings et al., 2012). Overpressured fluids could result from either dehydration of the oceanic crust (e.g. Kodaira et al., 2004) or the smectite–illite transition at 100–150 °C (Moore and Saffer, 2001). Based on a thermal model for South Central Chile (Völker et al., 2011), the temperature of this phase transformation coincides with the eastward limit of the frontal prism.

7.1.3. Continental forearc

The upper continental forearc (labelled '*cf*') beneath the Coastal Cordillera has a moderate v_p of 5.5–7.0 km/s and reduced v_p/v_s ratio of ~1.71 (Poisson's ratio of 0.24), consistent with a granitic composition (Christensen, 1996). This interpretation is supported by the widespread outcrops of granite across the Coastal Cordillera (Fig. 1) that likely extend through the upper crust (Groß and Micksch, 2008). Such velocities could also correspond to metabasite and metagreywacke compositions of the Western and Eastern Series, respectively (Christensen, 1996; Krawczyk et al., 2006). In the shallow crust (<10 km depth), low v_p (<6 km/s) corresponds to sediments in the Central Depression (labelled '*cd*').

In the lower forearc, prominent high v_p anomalies (7.6–8.0 km/s) lie beneath the coast. One is located at 36°S (hereafter referred to as the Cobquecura anomaly; labelled '*CA*'); the other to the north at 34°S (hereafter referred to as the Pichilemu anomaly; labelled '*PA*'), (Figs. 7 and 8). Based on the 7.5 km/s v_p contour, the Cobquecura anomaly is up to 40 km wide and 20 km thick, intersecting the plate interface at its base. This anomaly represents a significant velocity increase of 8% relative to the input 2-D model (Fig. S5). The smaller Pichilemu anomaly lies further above the plate interface. Crucially, both anomalies have a slightly elevated v_p/v_s ratio of ~1.81 (Poisson's ratio of 0.28) and a strong positive signature in the forearc Bouguer gravity field, which helps to constrain their composition. More specifically, there is a moderate positive correlation between gravity and v_p in the lower forearc (Fig. 8b).

Interpretation of the seismic velocities and gravity signal associated with the Cobquecura and Pichilemu anomalies clearly indicates dense, ultramafic material. Weakly-serpentinised peridotite (<20%) at these depths can explain the velocities (Christensen, 2004). Serpentinised peridotite at the continental forearc's base could represent a subducted oceanic topographic high, such as a seamount. However, our improved velocity model indicates that the Cobquecura anomaly is larger and seismically faster than previously thought (Hicks et al., 2012). Given these findings, we find a seamount interpretation less plausible. Dense material in the lower forearc could be a deeper manifestation of the Paleozoic granite batholith; however, the elevated v_p/v_s ratio rules out the possibility of residual intrusive material lying at its base (Husen et al., 2000; Reyners et al., 2006).

The surface projection of the ultramafic bodies corresponds reasonably well with the location of Triassic intrusions (Fig. S7). South of 37.5°S, a notable absence of high velocity bodies (Haberland et al., 2009) is consistent with a lack of Triassic intrusions in this region (Fig. 1). In contrast to the Paleozoic granites, these intrusions contain a stronger mantle source signature (Vásquez et al., 2011), possibly relating to the underlying ultramafic bodies. The Triassic intrusions were emplaced during extension (Vásquez et al., 2011) that was facilitated by either slab detachment (Parada et al., 1999), asthenospheric upwelling (Franzese and Spalletti, 2001) or slab steepening (Vásquez et al., 2011). It is plausible that any of these mechanisms could have emplaced mantle material beneath the ancient volcanic arc; remnants of this material could now lie at the base of the present-day forearc.

Interpreting which mechanism is responsible for the emplacement of these anomalous blocks of mantle material depends on their regional extent. Although large outcrops of Triassic intrusives have been mapped north of the Maule segment, in the Valparaiso area (Fig. 1), they do not extend south of the Maule segment. Given the discrete nature of these blocks, it is possible that the tectonic process responsible for their emplacement was more localised and limited to the central Chile region. Understanding the structure and petrology of such localised blocks of mantle material in the lower forearc crust could provide constraints on the genesis of arc magmas and could decipher models of localised slab processes, such as slab melting.

7.1.4. Continental mantle

Beneath the easternmost Coastal Cordillera, at depths of 25–35 km, v_p exceeds 7.25 km/s, defining a dome-shaped feature that

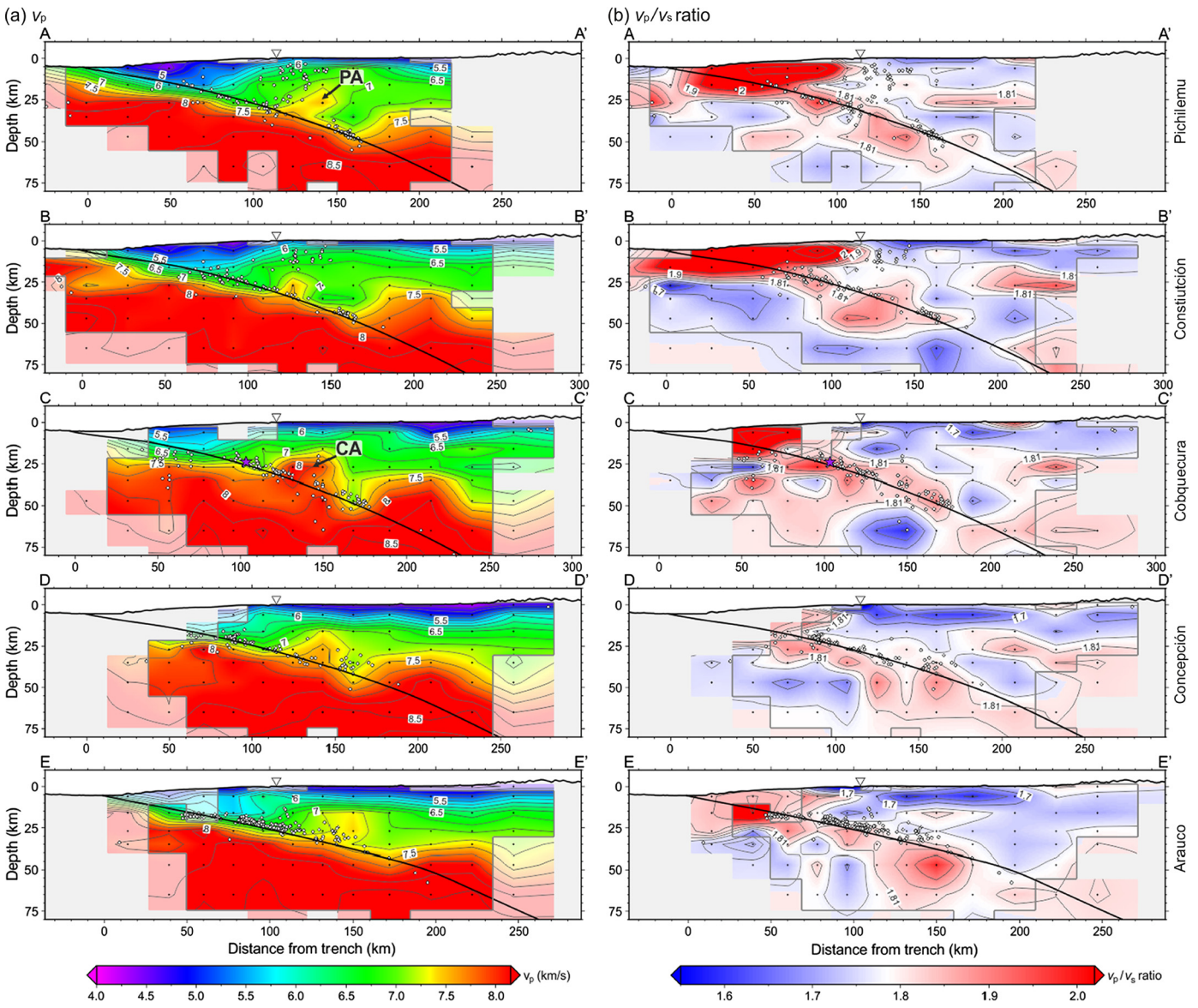

Fig. 7. 3-D velocity model plotted along five cross-sections, of which the locations are labelled on the far right and shown in Fig. 2. Labels refer to the following features that are discussed in the text: PA = Pichilemu anomaly; CA = Cobquecura anomaly. Resolution limits are defined in the same way as Fig. 6. The location of the coastline is denoted by the white triangle.

is present along the margin (labelled '*cm*'). Its location, regional geometry and velocity suggest that it represents the continental mantle wedge. Low-moderate v_p/v_s ratios of ~1.76 (Poisson's ratio of 0.26) in its western part are indicative of unserpentinised mantle (Carlson and Miller, 2003). Beneath the magmatic arc, we observe areas of elevated v_p/v_s, suggesting hydrated asthenospheric mantle, although its extent is unresolved.

By inspection of the velocity contours that intersect the plate interface, we find that the continental Moho, represented by a v_p of ~7.75 km/s, intersects the subducting plate interface at a depth of 45–50 km. This depth estimate is similar to that of Bohm (2004) and Haberland et al. (2009), but deeper than that of Dannowski et al. (2013). From our perspective, high v_p anomalies in the lower forearc could contaminate the lower resolution and laterally averaged receiver function image, resulting in a misplaced continental Moho.

7.1.5. Plate interface zone

The curved region of seismicity, dipping away from the trench, defines the plate interface. To define geometry of the fault, we selected all events that lie within ±15 km depth of previous plate interface estimates (e.g. Haberland et al., 2009; Hayes et al., 2012), fitting a second-order polynomial through these events. Since seismicity did not reach the trench, we fixed the shallowest part of the interface to the trench at 7 km depth (e.g. Contreras Reyes et al., 2008). In 3-D, we followed a similar workflow proposed by Hayes and Wald (2009). We find that our revised interface geometry (Figs. 6, 7 and Fig. S7) corresponds to the mean depth of thrust mechanism aftershocks (Agurto et al., 2012; Hayes et al., 2013), (Fig. S8). By projecting this interface through our 3-D velocity model, we can assess the velocity structure of the plate interface. To account for both hypocentre and velocity uncertainties, we estimate the error in plate interface velocity (see Note S1).

The velocity structure of the plate interface region shows a clear zonation of seismic properties with depth (Fig. 9 and Fig. S9). Given the spacing of nodes with depth, (see Section 5.2), our model represents the average plate interface velocity over a total thickness of 6–8 km. Therefore, any thin (<4 km thick) low velocity layers along the plate interface (e.g. Haberland et al., 2009) are unlikely to be imaged. Along the shallowest part of the plate interface, beneath the frontal prism, v_p is relatively low (~6.6 km/s)

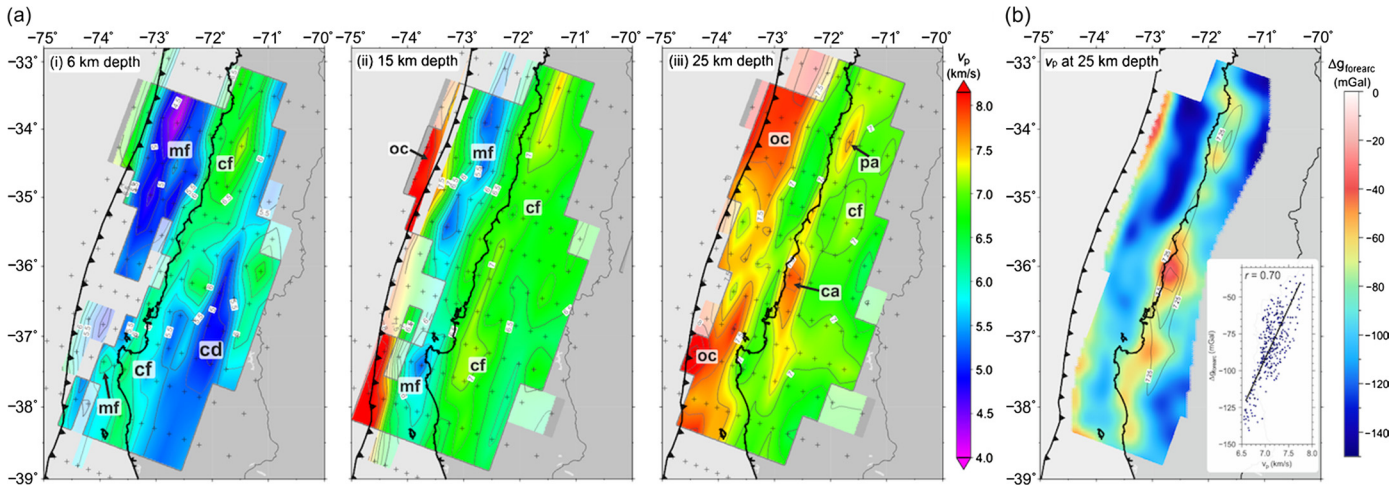

Fig. 8. (a) 3-D velocity model plotted as depth sections. Labels refer to the following features that are discussed in the text: mf = marine forearc; oc = oceanic crust; cf = upper forearc crust; cd = Central Depression; PA = Pichilemu anomaly; CA = Cobquecura anomaly. Resolution limits are defined in the same way as Fig. 6. (b) Forearc Bouguer gravity anomaly (Hicks et al., 2012) overlain by contours of v_p model at 25 km depth. Contours are given for v_p in the range 7.25–8 km/s. Inset: scatter plot showing the correlation between forearc Bouguer gravity anomaly and forearc v_p at 25 km, sampled at 0.2° intervals of latitude and longitude.

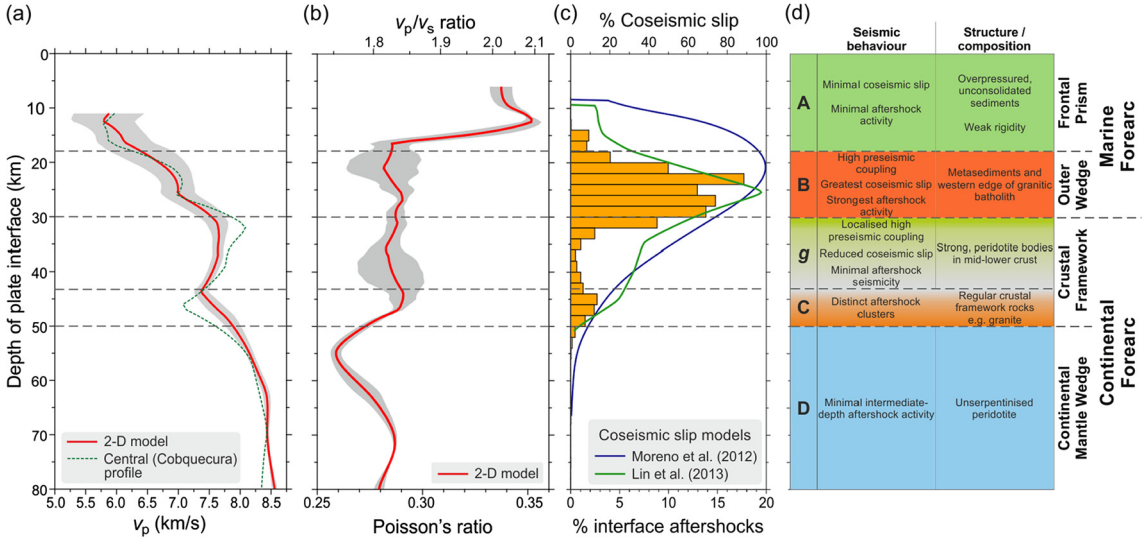

Fig. 9. Seismic velocities along the plate interface from the 2-D model plotted as a function of depth for (a) v_p and (b) v_p/v_s ratio. Grey shading shows our estimated uncertainty in these seismic velocities. (c) Histogram of plate interface aftershock earthquake depths and normalised coseismic slip distribution as a function of depth. Trench-perpendicular slip profiles traverse the northern slip asperity. Aftershock hypocentres are relocated from the catalogue of Rietbrock et al. (2012). (d) Depth-segmentation of the plate interface region based on interpretation of the seismic velocities and seismic character of the Maule megathrust. Letters in the left-hand column correspond to the megathrust domains of Lay et al. (2012).

and v_p/v_s ratio is high (1.87–2.05). Beneath the outer wedge, v_p sharply increases with depth (~0.03 km/s per km) and v_p/v_s ratio decreases to ~1.84. Beneath the lower forearc crust, v_p levels out at ~7.5 km/s, but reaches up to 8 km/s where the plate interface intersects the high velocity bodies (Fig. 9a). At depths of ~44 km, v_p decreases to ~7.4 km/s. Beneath the Central Depression, v_p further increases to ~8.5 km/s and v_p/v_s ratio decreases to ~1.78. Given this segmented velocity structure of the plate interface, the next logical step is to consider whether this influences megathrust behaviour.

7.2. Correlating megathrust behaviour with plate interface velocity structure

7.2.1. Preseismic coupling of the megathrust

Based on the preseismic locking model of Moreno et al. (2010), the Maule megathrust before the 2010 earthquake was strongly coupled (>90%) beneath the outer wedge, where the plate interface has moderate v_p (6.25–7 km/s) and elevated v_p/v_s ratio of 1.88 (Fig. 10a). The interface was also strongly locked (>90%) beneath the coast, at the base of the Cobquecura ultramafic body. For the Arauco peninsula region, Moreno et al. (2014) identify a correlation between weakly locked regions of the interface and elevated v_p/v_s ratio due to high fluid pressures. We also find a strong correlation ($r = -0.71$) for the region south of 37°S (Fig. S12). However, we do not find such a clear correlation for the whole rupture zone (Fig. S11a). This finding indicates that factors controlling preseismic locking may change across the Maule segment.

7.2.2. Nucleation and rupture of the Maule earthquake

The Maule earthquake nucleated in a region of high v_p (~7.2 km/s) and strong dip-parallel v_p gradient, at the periphery of the Cobquecura anomaly (Fig. 10b). This inference is in line with Tassara (2010), who shows that ruptures along the Andean margin generally nucleate at the edge of geological heterogeneities

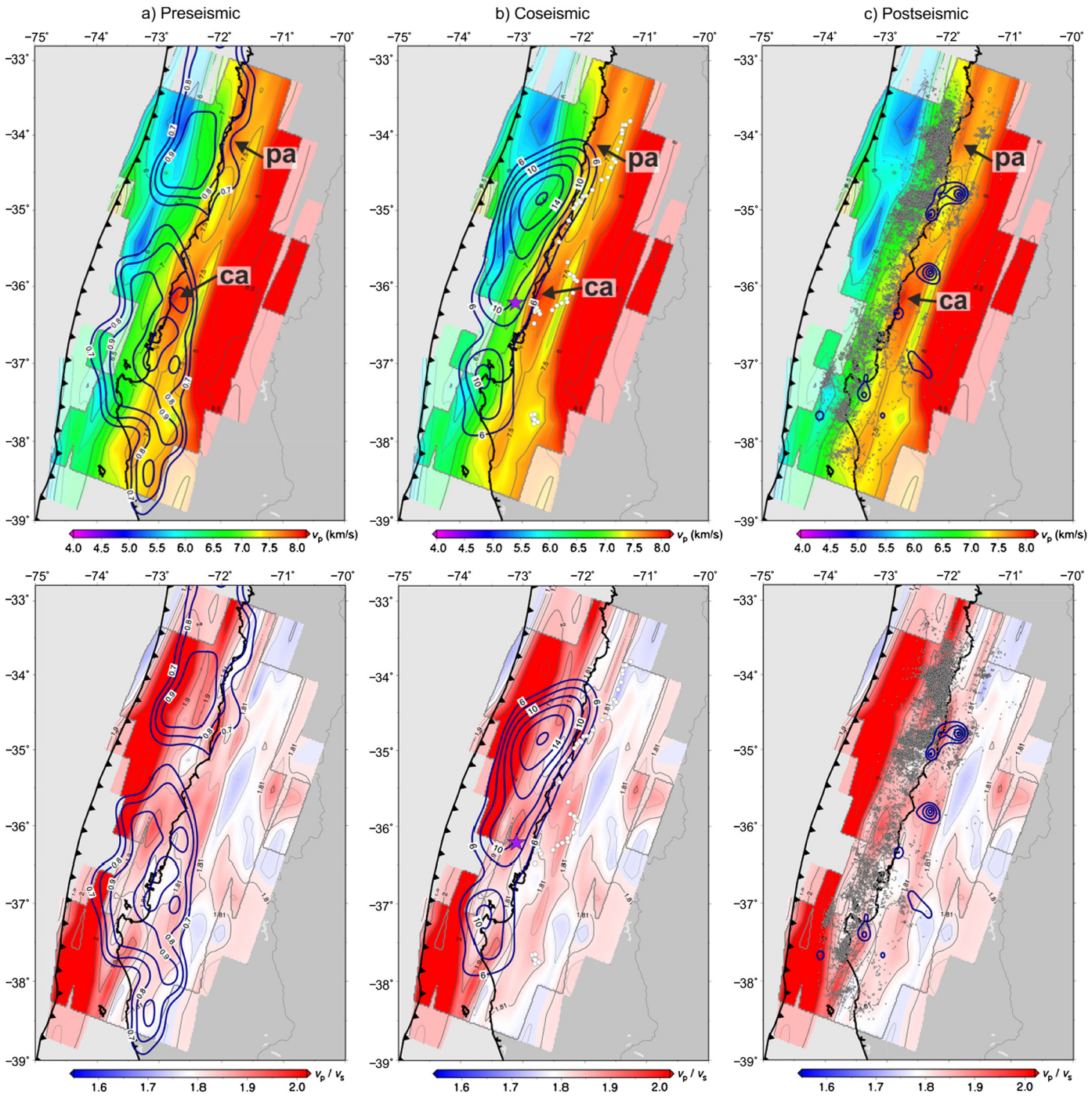

Fig. 10. Distribution of (top) v_p and (bottom) v_p/v_s ratio along the plate interface region compared with behaviour of the Maule megathrust over the seismic cycle. Labels refer to the features discussed in the text and are defined in the caption of Fig. 7. (a) Contours of preseismic locking of the megathrust (Moreno et al., 2010) (blue lines) are for locking of greater than 0.7 and given in intervals of 0.1. (b) Mainshock epicentral location from Hayes et al. (2013). Coseismic slip distribution (Moreno et al., 2012) plotted as for Fig. 2. White circles give the location of high frequency energy release during the Maule earthquake (Kiser and Ishii, 2011). (c) Contours of afterslip >1 m (Lin et al., 2013) (blue lines) plotted in 0.2 m intervals. Grey circles show the distribution of relocated plate interface aftershock seismicity. (For interpretation of the references to colour in this figure legend, the reader is referred to the web version of this article.)

in the forearc. A local increase in stress at the edge the Cobquecura anomaly could have led to onset of the rupture.

Following nucleation, most coseismic slip occurred along the plate interface beneath the outer wedge, where we find moderate v_p (~6.5 km/s) and elevated v_p/v_s ratio (~1.86), (Figs. 9 and 10b). Coseismic slip was minimal beneath the frontal prism ($v_p < 6.25$ km/s; v_p/v_s ratio >1.85) and beneath the continental mantle wedge ($v_p > 7.5$ km/s; v_p/v_s ratio <1.8). Coseismic slip was reduced beneath the crustal forearc where v_p becomes more than 7.25 km/s. The northern and southern slip asperities correspond to weaker v_p gradient with depth. This more homogeneous velocity structure is partly due to the lack of high v_p anomalies beneath the coast in the Constitución and Arauco regions. Therefore, it is possible that slip localisation during the Maule earthquake was affected by the presence of long-lived mafic bodies in the lower forearc. Overall, there is strong negative correlation between v_p and coseismic slip for the down-dip portion of the rupture (Fig. S13).

At shallow depths along the fault (<17 km), coseismic slip was reduced by 50% (Lin et al., 2013). At these depths, v_p sharply decreases and v_p/v_s ratio abruptly increases to >2 (Fig. 9). Comparison of slip with seismic velocity at shallow depths suggests that overpressure conditions (Spinelli et al., 2006) and material with low rigidity at the base of the frontal prism inhibited slip. The smectite–illite transition may contribute to this overpressure (Moore and Saffer, 2001) and influence the transition between velocity strengthening and velocity weakening regimes (e.g. Saffer and Marone, 2003).

For the high frequency part of the rupture (Kiser and Ishii, 2011), there is a striking interaction with velocity structure along the plate interface (Fig. 10b). The locations of high frequency energy release appear to step down around the high velocity anomalies, with most energy coming from deeper regions of the plate interface that have intermediate v_p and elevated v_p/v_s ratio. High frequency energy release during an earthquake can be caused by sudden changes in rupture speed or slip (Madariaga, 1977). Based on the coseismic slip distribution (Moreno et al., 2012), we propose that the rupture was slowed by the high velocity anomalies beneath the coast, generating stopping phases at the rupture's down-dip termination.

7.2.3. Postseismic deformation following the Maule earthquake

To investigate the relationship between velocity structure and aftershock seismicity, we relocated the full 2010 aftershock catalogue of Rietbrock et al. (2012), (see Supplementary Note 2 for a discussion of how combining OBS data with high-quality, manually determined onset times affects earthquake locations). We find that the Cobquecura and Pichilemu anomalies clearly lie within the distinct gap of plate interface aftershock seismicity (Fig. 10c and Fig. S15). Intense crustal seismicity also occurred along the western edge of the Pichilemu anomaly. It is plausible that structural heterogeneity in the lower forearc influenced the distribution of plate interface and shallow crustal seismicity following the Maule earthquake. Tomographic images from Japan also show a similar relationship between crustal high velocities and aftershock seismicity (Kato et al., 2010, 2013). Significant afterslip occurred in regions of intermediate plate interface v_p (7.2–7.5 km/s) and elevated v_p/v_s ratio (1.82–1.84) (Fig. 10c and Fig. S10c). This finding suggests that afterslip following the Maule earthquake may have been compositionally driven.

7.3. Depth-varying rupture properties and fault material properties

Based on the depth variation of subduction zone rupture characteristics, Lay et al. (2012) classify the megathrust into four distinct domains (A–D). From the physical properties and seismogenic characteristics of the Maule megathrust, we can draw parallels with this classification (Fig. 9c). The plate interface beneath the frontal prism (<17 km depth) was largely aseismic during the Maule rupture, corresponding to Domain A. The high v_p/v_s and Poisson's ratios provide direct evidence for low rigidity material existing at shallow depths that was proposed by Bilek and Lay (1999) to influence aseismic behaviour and occasional slow, tsunamigenic earthquakes. The depth of the plate interface beneath the outer wedge (17–30 km) corresponds to Domain B, the most seismogenic part of the megathrust. For the Maule earthquake, the greatest coseismic slip and aftershock activity occurred in this domain, and is where the plate interface is structurally more homogeneous.

Domain C should theoretically lie at 35–55 km depth beneath the continental forearc. However, at 30–44 km depth, where the plate interface intersects ultramafic bodies in the lower forearc, coseismic slip was reduced and postseismic slip was minimal; such seismic characteristics deviate from Domain C. Therefore, we instead propose a new domain, 'g', for the Maule megathrust. At greater depths (44–50 km), the predominance of high frequency radiation and localised aftershock clusters agrees well with Domain C, where v_p indicates a return to normal interface structure. It has been proposed that the maximum depth of the seismogenic zone is influenced by the intersection of the 350–450 °C isotherm with the plate interface (e.g. Hyndman et al., 1997). Based on Völker et al. (2011) however, these temperatures are not reached until 65–90 km depth, so temperature is unlikely to play a role in the deeper segmentation of the Maule megathrust.

8. Conclusions

In this paper, we have presented a detailed seismic velocity model (v_p and v_p/v_s ratio) of the 2010 M_w 8.8 Maule, Chile earthquake rupture zone. A dense aftershock dataset from onshore and offshore seismic networks allowed an in-depth study of physical properties along the megathrust interface and in the overlying forearc.

Our velocity model shows that two high velocity anomalies with $v_p > 7.5$ km/s lie beneath the coast, at the base of the continental forearc in the central and northern parts of the rupture zone. We interpret these high velocity anomalies as large (up to 15 km thick), dense bodies of ultramafic peridotite. A comparison with the surface geology suggests that these bodies could be relic blocks of mantle.

By comparing the location of these anomalous bodies with the behaviour of the earthquake, we show that they may have played a role in controlling the down-dip and along-strike distribution of slip during the rupture. It also appears that these anomalies influenced the location of high frequency seismic energy. Hence, long-lived structural and compositional heterogeneities in the forearc can act as a rupture barrier during large earthquakes and can influence the along-strike segmentation of ruptures along the Central Chile margin. These ultramafic blocks are also associated with a distinct gap in plate interface aftershock seismicity. The Pichilemu velocity anomaly acted as a structural discontinuity, influencing the focus of normal faulting aftershock seismicity in the overriding crust. At the shallow end of the seismogenic zone, overpressured, low rigidity sediments at the base of the frontal prism likely inhibited shallow rupture during the Maule earthquake. The megathrust fault beneath the Cobquecura anomaly was strongly locked before the Maule earthquake, yet experienced little coseismic slip. This part of the fault was therefore recognised by Moreno et al. (2012) as experiencing slip deficit. Since this study, there has been minimal postseismic slip along this portion of the fault, raising questions over the current state of stress and overall rheological nature of the Cobquecura anomaly.

Overall, P-wave velocities of greater than 7.5 km/s inhibited seismic and aseismic slip both during and after the Maule earthquake. Therefore, an understanding of physical properties along the plate interface could help in determining the seismic hazard of a subduction zone. Seismic velocity could be used as a proxy in other subduction zones to estimate rupture size potential and the regions conducive to high frequency seismic energy release and localisation of shallow crustal aftershock seismicity.

Acknowledgements

The IMAD dataset is available through IRIS and GFZ (http://www.iris.edu/dms/dmc; http://www.webdc.eu). We are grateful to all field crews that participated in the onshore and offshore deployments. We thank IRIS/PASSCAL, CNRS-INSU, GFZ and GEF/SEIS-UK for providing the onshore seismic instruments. The Universidad

de Chile and Universidad de Concepción provided valuable support in the field, and we are also grateful to the CAP/OSU/IGM GPS teams for advice and logistical assistance. The National Taiwan Ocean University and UK Ocean Bottom Instrument Consortium (OBIC) provided OBS instruments. Dr. Victor Ariel Gallardo (Oceanography Department, Universidad de Concepción), Captain Juan Vilches and Freddy Echeverria provided vital logistics support for the offshore deployment. We are grateful to the Armada de Chile for providing vessels. NERC funded the UK deployments (grant NE/I005420/1). Amaya Fuenzalida provided insightful comments on the manuscript. S.P.H. is funded by a NERC studentship, NE/J50015X/1. We thank the editor and two anonymous reviewers for their insightful comments.

Appendix A. Supplementary material

Supplementary material related to this article can be found online at http://dx.doi.org/10.1016/j.epsl.2014.08.028.

References

Abercrombie, R.E., Antolik, M., Felzer, K., Ekström, G., 2001. The 1994 Java tsunami earthquake: slip over a subducting seamount. J. Geophys. Res. 106, 6595–6607. http://dx.doi.org/10.1029/2000JB900403.

Agurto, H., Rietbrock, A., Ryder, I., Miller, M., 2012. Seismic-afterslip characterization of the 2010 *Mw* 8.8 Maule, Chile, earthquake based on moment tensor inversion. Geophys. Res. Lett. 39, L20303. http://dx.doi.org/10.1029/2012GL053434.

Audin, L., Lacan, P., Tavera, H., Bondoux, F., 2008. Upper plate deformation and seismic barrier in front of Nazca subduction zone: the Chololo Fault System and active tectonics along the Coastal Cordillera, southern Peru. Tectonophysics 459, 174–185. http://dx.doi.org/10.1016/j.tecto.2007.11.070.

Bedford, J., Moreno, M., Baez, J.C., Lange, D., Tilmann, F., Rosenau, M., Heidbach, O., Oncken, O., Bartsch, M., Rietbrock, A., Tassara, A., Bevis, M., Vigny, C., 2013. A high-resolution, time-variable afterslip model for the 2010 Maule $Mw = 8.8$, Chile megathrust earthquake. Earth Planet. Sci. Lett. 383, 26–36. http://dx.doi.org/10.1016/j.epsl.2013.09.020.

Bilek, S.L., Lay, T., 1999. Rigidity variations with depth along interplate megathrust faults in subduction zones. Nature 400, 443–446. http://dx.doi.org/10.1038/22739.

Bohm, M., 2004. 3-D Lokalbebentomographie der sudlichen Anden zwischen 36° und 40°S. Freie Universitat, Berlin, Germany.

Calvert, A., Sandvol, E., Seber, D., Barazangi, M., Roecker, S., Mourabit, T., Vidal, F., Alguacil, G., Jabour, N., 2000. Geodynamic evolution of the lithosphere and upper mantle beneath the Alboran region of the western Mediterranean: constraints from travel time tomography. J. Geophys. Res. 105, 10871–10898. http://dx.doi.org/10.1029/2000JB900024.

Carlson, R.L., Miller, D.J., 2003. Mantle wedge water contents estimated from seismic velocities in partially serpentinized peridotites. Geophys. Res. Lett. 30, 51–54. http://dx.doi.org/10.1029/2002GL016600.

Chen, A.T., Frohlich, C., Latham, G.V., 1982. Seismicity of the forearc marginal wedge (accretionary prism). J. Geophys. Res. 87, 3679–3690. http://dx.doi.org/10.1029/JB087iB05p03679.

Christensen, N.I., 1996. Poisson's ratio and crustal seismology. J. Geophys. Res. 101, 3139–3156. http://dx.doi.org/10.1029/95JB03446.

Christensen, N.I., 2004. Serpentinites, peridotites, and seismology. Int. Geol. Rev. 46, 795–816. http://dx.doi.org/10.2747/0020-6814.46.9.795.

Collings, R., Lange, D., Rietbrock, A., Tilmann, F., Natawidjaja, D., Suwargadi, B., Miller, M., Saul, J., 2012. Structure and seismogenic properties of the Mentawai segment of the Sumatra subduction zone revealed by local earthquake traveltime tomography. J. Geophys. Res. 117, B01312. http://dx.doi.org/10.1029/2011JB008469.

Contreras Reyes, E., Grevemeyer, I., Flueh, E.R., Reichert, C., 2008. Upper lithospheric structure of the subduction zone offshore of southern Arauco peninsula, Chile, at ~38°S. J. Geophys. Res. 113, B07303. http://dx.doi.org/10.1029/2007JB005569.

Contreras-Reyes, E., Jara, J., Maksymowicz, A., Weinrebe, W., 2013. Sediment loading at the southern Chilean trench and its tectonic implications. J. Geodyn. 66, 134–145. http://dx.doi.org/10.1016/j.jog.2013.02.009.

Dannowski, A., Grevemeyer, I., Kraft, H., Arroyo, I., Thorwart, M., 2013. Crustal thickness and mantle wedge structure from receiver functions in the Chilean Maule region at 35°S. Tectonophysics 592, 159–164. http://dx.doi.org/10.1016/j.tecto.2013.02.015.

DeMets, C., Gordon, R.G., Argus, D.F., 2010. Geologically current plate motions. Geophys. J. Int. 181, 1–80. http://dx.doi.org/10.1111/j.1365-246X.2009.04491.x.

Eberhart Phillips, D., 1986. Three-dimensional velocity structure in northern California Coast Ranges from inversion of local earthquake arrival times. Bull. Seismol. Soc. Am. 76, 1025–1052.

Eberhart Phillips, D., Michael, A.J., 1998. Seismotectonics of the Loma Prieta, California, region determined from three-dimensional V_p, V_p/V_s, and seismicity. J. Geophys. Res. 103, 21099. http://dx.doi.org/10.1029/98JB01984.

Eberhart Phillips, D., Reyners, M., Chadwick, M., Chiu, J.M., 2005. Crustal heterogeneity and subduction processes: 3-D V_p, V_p/V_s and Q in the southern North Island, New Zealand. Geophys. J. Int. 162, 270–288. http://dx.doi.org/10.1111/j.1365-246X.2005.02530.x.

Franzese, J.R., Spalletti, L.A., 2001. Late Triassic–early Jurassic continental extension in southwestern Gondwana: tectonic segmentation and pre-breakup rifting. J. South Am. Earth Sci. 14, 257–270. http://dx.doi.org/10.1016/S0895-9811(01)00029-3.

Frohlich, C., Billington, S., Engdahl, E.R., Malahoff, A., 1982. Detection and location of earthquakes in the Central Aleutian Subduction Zone using island and ocean bottom seismograph stations. J. Geophys. Res. 87, 6853–6864. http://dx.doi.org/10.1029/JB087iB08p06853.

Fuller, C.W., Willett, S.D., Brandon, M.T., 2006. Formation of forearc basins and their influence on subduction zone earthquakes. Geology 34, 65–68. http://dx.doi.org/10.1130/g21828.1.

Glodny, J., Gräfe, K., Echtler, H., Rosenau, M., 2007. Mesozoic to Quaternary continental margin dynamics in South-Central Chile (36–42°S): the apatite and zircon fission track perspective. Int. J. Earth Sci. 97, 1271–1291. http://dx.doi.org/10.1007/s00531-007-0203-1.

Groß, K., Micksch, U., 2008. The reflection seismic survey of project TIPTEQ—the inventory of the Chilean subduction zone at 38.2°S. Geophys. J. Int. http://dx.doi.org/10.1111/j.1365-246X.2007.03680.x.

Haberland, C., Rietbrock, A., Lange, D., Bataille, K., Dahm, T., 2009. Structure of the seismogenic zone of the southcentral Chilean margin revealed by local earthquake traveltime tomography. J. Geophys. Res. 114, B01317. http://dx.doi.org/10.1029/2008jb005802.

Haberland, C., Rietbrock, A., Lange, D., Bataille, K., Hofmann, S., 2006. Interaction between forearc and oceanic plate at the south-central Chilean margin as seen in local seismic data. Geophys. Res. Lett. 33. http://dx.doi.org/10.1029/2006GL028189.

Hacker, B.R., Abers, G.A., 2004. Subduction Factory 3: an Excel worksheet and macro for calculating the densities, seismic wave speeds, and H_2O contents of minerals and rocks at pressure and temperature. Geochem. Geophys. Geosyst. 5, Q01005. http://dx.doi.org/10.1029/2003GC000614.

Hayes, G.P., Bergman, E., Johnson, K.L., Benz, H.M., Brown, L., Meltzer, A.S., 2013. Seismotectonic framework of the 2010 February 27 M_w 8.8 Maule, Chile earthquake sequence. Geophys. J. Int. 195, 1034–1051. http://dx.doi.org/10.1093/gji/ggt238.

Hayes, G.P., Wald, D.J., 2009. Developing framework to constrain the geometry of the seismic rupture plane on subduction interfaces a priori—a probabilistic approach. Geophys. J. Int. 176, 951–964. http://dx.doi.org/10.1111/j.1365-246X.2008.04035.x.

Hayes, G.P., Wald, D.J., Johnson, R.L., 2012. Slab1.0: a three-dimensional model of global subduction zone geometries. J. Geophys. Res. 117. http://dx.doi.org/10.1029/2011JB008524.

Hicks, S.P., Rietbrock, A., Haberland, C.A., Ryder, I.M.A., Simons, M., Tassara, A., 2012. The 2010 M_w 8.8 Maule, Chile earthquake: nucleation and rupture propagation controlled by a subducted topographic high. Geophys. Res. Lett. 39. http://dx.doi.org/10.1029/2012GL053184.

Husen, S., Kissling, E., Flueh, E., Asch, G., 1999. Accurate hypocentre determination in the seismogenic zone of the subducting Nazca Plate in northern Chile using a combined on-/offshore network. Geophys. J. Int. 138, 687–701. http://dx.doi.org/10.1046/j.1365-246x.1999.00893.x.

Husen, S., Kissling, E., Flueh, E.R., 2000. Local earthquake tomography of shallow subduction in north Chile: a combined onshore and offshore study. J. Geophys. Res. 105, 28183–28198. http://dx.doi.org/10.1029/2000JB900229.

Hyndman, R., Yamano, M., Oleskevich, D., 1997. The seismogenic zone of subduction thrust faults. Isl. Arc 6, 244–260. http://dx.doi.org/10.1111/j.1440-1738.1997.tb00175.x.

Kato, A., Igarashi, T., Obara, K., Sakai, S., Takeda, T., Saiga, A., Iidaka, T., Iwasaki, T., Hirata, N., Goto, K., Miyamachi, H., Matsushima, T., Kubo, A., Katao, H., Yamanaka, Y., Terakawa, T., Nakamichi, H., Okuda, T., Horikawa, S., Tsumura, N., Umino, N., Okada, T., Kosuga, M., Takahashi, H., Yamada, T., 2013. Imaging the source regions of normal faulting sequences induced by the 2011 M9.0 Tohoku-Oki earthquake. Geophys. Res. Lett. 40, 273–278. http://dx.doi.org/10.1002/grl.50104.

Kato, A., Miyatake, T., Hirata, N., 2010. Asperity and barriers of the 2004 Mid-Niigata Prefecture earthquake revealed by highly dense seismic observations. Bull. Seismol. Soc. Am. 100, 298–306. http://dx.doi.org/10.1785/0120090218.

Kiser, E., Ishii, M., 2011. The 2010 M_w 8.8 Chile earthquake: triggering on multiple segments and frequency-dependent rupture behavior. Geophys. Res. Lett. 38, L07301. http://dx.doi.org/10.1029/2011GL047140.

Kissling, E., Ellsworth, W.L., Eberhart-Phillips, D., Kradolfer, U., 1994. Initial reference models in local earthquake tomography. J. Geophys. Res. 99, 19635–19646. http://dx.doi.org/10.1029/93JB03138.

Kodaira, S., Iidaka, T., Kato, A., Park, J.O., Iwasaki, T., Kaneda, Y., 2004. High pore fluid pressure may cause silent slip in the Nankai Trough. Science 304, 1295–1298. http://dx.doi.org/10.1126/science.1096535.

Krawczyk, C.M., Mechie, J., Lüth, S., Tašárová, Z., Wigger, P., Stiller, M., Brasse, H., Echtler, H.P., Araneda, M., Bataille, K., 2006. Geophysical signatures and active tectonics at the South-Central Chilean margin. In: The Andes Active Subduction Orogeny. Springer, New York, pp. 171–192.

Lange, D., Tilmann, F., Barrientos, S.E., Contreras-Reyes, E., Methe, P., Moreno, M., Heit, B., Agurto, H., Bernard, P., Vilotte, J.-P., 2012. Aftershock seismicity of the 27 February 2010 *Mw* 8.8 Maule earthquake rupture zone. Earth Planet. Sci. Lett. 317–318, 413–425. http://dx.doi.org/10.1016/j.epsl.2011.11.034.

Lay, T., Kanamori, H., 1981. An asperity model of large earthquake sequences. In: Maurice Ewing Series: Earthquake Prediction: An International Review. Washington, DC, pp. 579–592.

Lay, T., Kanamori, H., Ammon, C.J., Koper, K.D., Hutko, A.R., Ye, L., Yue, H., Rushing, T.M., 2012. Depth-varying rupture properties of subduction zone megathrust faults. J. Geophys. Res. 117, B04311. http://dx.doi.org/10.1029/2011JB009133.

Lee, W.H.K., Valdes, C., 1985. HYPO71PC: a personal computer version of the HYPO71 earthquake location program. U.S. Geol. Surv. Open File Rep., 85–749.

Lin, Y.N., Sladen, A., Ortega-Culaciati, F., Simons, M., Avouac, J.-P., Fielding, E.J., Brooks, B.A., Bevis, M., Genrich, J., Rietbrock, A., 2013. Coseismic and postseismic slip associated with the 2010 Maule Earthquake, Chile: characterizing the Arauco Peninsula barrier effect. J. Geophys. Res. 118 (6), 3142–3159. http://dx.doi.org/10.1002/jgrb.50207.

Lucassen, F., Trumbull, R., Franz, G., Creixell, C., Vásquez, P., Romer, R.L., Figueroa, O., 2004. Distinguishing crustal recycling and juvenile additions at active continental margins: the Paleozoic to recent compositional evolution of the Chilean Pacific margin (36–41°S). J. South Am. Earth Sci. 17, 103–119. http://dx.doi.org/10.1016/j.jsames.2004.04.002.

Madariaga, R., 1977. High-frequency radiation from crack (stress drop) models of earthquake faulting. Geophys. J. Int. 51, 625–651. http://dx.doi.org/10.1111/j.1365-246X.1977.tb04211.x.

Martin, M.W., Kato, T.T., Rodriguez, C., Godoy, E., Duhart, P., McDonough, M., Campos, A., 1999. Evolution of the late Paleozoic accretionary complex and overlying forearc-magmatic arc, south central Chile (38°–41°S): constraints for the tectonic setting along the southwestern margin of Gondwana. Tectonics 18, 582–605. http://dx.doi.org/10.1029/1999TC900021.

Melnick, D., Echtler, H.P., 2006. Morphotectonic and geologic digital map compilations of the South-Central Andes (36°–42°S). In: The Andes. Springer, Berlin, Heidelberg, pp. 565–568.

Métois, M., Socquet, A., Vigny, C., 2012. Interseismic coupling, segmentation and mechanical behavior of the central Chile subduction zone. J. Geophys. Res. 117, B03406. http://dx.doi.org/10.1029/2011JB008736.

Moore, J.C., Saffer, D., 2001. Updip limit of the seismogenic zone beneath the accretionary prism of southwest Japan: an effect of diagenetic to low-grade metamorphic processes and increasing effective stress. Geology 29, 183–186. http://dx.doi.org/10.1130/0091-7613(2001)029<0183:ULOTSZ>2.0.CO;2.

Moreno, M., Haberland, C., Oncken, O., Rietbrock, A., Angiboust, S., Heidbach, O., 2014. Locking of the Chile subduction zone controlled by fluid pressure before the 2010 earthquake. Nat. Geosci. 7, 292–296. http://dx.doi.org/10.1038/ngeo2102.

Moreno, M., Melnick, D., Rosenau, M., Baez, J., Klotz, J., Oncken, O., Tassara, A., Chen, J., Bataille, K., Bevis, M., Socquet, A., Bolte, J., Vigny, C., Brooks, B., Ryder, I., Grund, V., Smalley, B., Carrizo, D., Bartsch, M., Hase, H., 2012. Toward understanding tectonic control on the M_w 8.8 2010 Maule Chile earthquake. Earth Planet. Sci. Lett. 321–322, 152–165. http://dx.doi.org/10.1016/j.epsl.2012.01.006.

Moreno, M., Rosenau, M., Oncken, O., 2010. 2010 Maule earthquake slip correlates with pre-seismic locking of Andean subduction zone. Nature 467, 198–202. http://dx.doi.org/10.1038/nature09349.

Moscoso, E., Grevemeyer, I., Contreras-Reyes, E., Flueh, E.R., Dzierma, Y., Rabbel, W., Thorwart, M., 2011. Revealing the deep structure and rupture plane of the 2010 Maule, Chile earthquake ($Mw = 8.8$) using wide angle seismic data. Earth Planet. Sci. Lett. 307, 147–155. http://dx.doi.org/10.1016/j.epsl.2011.04.025.

Parada, M.A., Nyström, J.O., Levi, B., 1999. Multiple sources for the Coastal Batholith of central Chile (31–34°S): geochemical and Sr–Nd isotopic evidence and tectonic implications. Lithos 46, 505–521. http://dx.doi.org/10.1016/S0024-4937(98)00080-2.

Reyners, M., Eberhart Phillips, D., Stuart, G., Nishimura, Y., 2006. Imaging subduction from the trench to 300 km depth beneath the central North Island, New Zealand, with V_p and V_p/V_s. Geophys. J. Int. 165, 565–583. http://dx.doi.org/10.1111/j.1365-246X.2006.02897.x.

Rietbrock, A., Ryder, I., Hayes, G., Haberland, C., Comte, D., Roecker, S., Lyon-Caen, H., 2012. Aftershock seismicity of the 2010 Maule $Mw = 8.8$, Chile, earthquake: correlation between co-seismic slip models and aftershock distribution? Geophys. Res. Lett. 39, L08310. http://dx.doi.org/10.1029/2012GL051308.

Ruegg, J.C., Rudloff, A., Vigny, C., Madariaga, R., De Chabalier, J.B., Campos, J., Kausel, E., Barrientos, S., Dimitrov, D., 2009. Interseismic strain accumulation measured by GPS in the seismic gap between Constitución and Concepción in Chile. Phys. Earth Planet. Inter. 175, 78–85. http://dx.doi.org/10.1016/j.pepi.2008.02.015.

Ryder, I., Rietbrock, A., Kelson, K., Bürgmann, R., Floyd, M., Socquet, A., Vigny, C., Carrizo, D., 2012. Large extensional aftershocks in the continental forearc triggered by the 2010 Maule earthquake, Chile. Geophys. J. Int. 188, 879–890. http://dx.doi.org/10.1111/j.1365-246X.2011.05321.x.

Saffer, D.M., Marone, C., 2003. Comparison of smectite- and illite-rich gouge frictional properties: application to the updip limit of the seismogenic zone along subduction megathrusts. Earth Planet. Sci. Lett. 215, 219–235. http://dx.doi.org/10.1016/S0012-821X(03)00424-2.

SERNAGEOMIN, 2003. Mapa Geológico de Chile: versión digital. Servicio Nacional de Geología y Minería, Santiago, Chile.

Sobiesiak, M., Meyer, U., Schmidt, S., Götze, H.J., Krawczyk, C.M., 2007. Asperity generating upper crustal sources revealed by *b* value and isostatic residual anomaly grids in the area of Antofagasta, Chile. J. Geophys. Res. 112, B12308. http://dx.doi.org/10.1029/2006JB004796.

Song, T., Simons, M., 2003. Large trench-parallel gravity variations predict seismogenic behavior in subduction zones. Science 301, 630. http://dx.doi.org/10.1126/science.1085557.

Spinelli, G.A., Saffer, D.M., Underwood, M.B., 2006. Hydrogeologic responses to three-dimensional temperature variability, Costa Rica subduction margin. J. Geophys. Res. 111, B04403. http://dx.doi.org/10.1029/2004JB003436.

Tassara, A., 2010. Control of forearc density structure on megathrust shear strength along the Chilean subduction zone. Tectonophysics 495, 34–47. http://dx.doi.org/10.1016/j.tecto.2010.06.004.

Thurber, C.H., 1983. Earthquake locations and three-dimensional crustal structure in the Coyote Lake area, central California. J. Geophys. Res. 88, 8226–8236. http://dx.doi.org/10.1029/JB088iB10p08226.

Thurber, C., Eberhart Phillips, D., 1999. Local earthquake tomography with flexible gridding. Comput. Geosci. 25, 809–818. http://dx.doi.org/10.1016/S0098-3004(99)00007-2.

Toomey, D.R., Foulger, G.R., 1989. Tomographic inversion of local earthquake data from the Hengill-Grensdalur Central Volcano Complex, Iceland. J. Geophys. Res. 94, 17497–17510. http://dx.doi.org/10.1029/JB094iB12p17497.

Tsuji, T., Tokuyama, H., Costa Pisani, P., Moore, G., 2008. Effective stress and pore pressure in the Nankai accretionary prism off the Muroto Peninsula, southwestern Japan. J. Geophys. Res. 113, B11401. http://dx.doi.org/10.1029/2007JB005002.

Vásquez, P., Franz, G., 2008. The Triassic Cobquecura Pluton (Central Chile): an example of a fayalite-bearing A-type intrusive massif at a continental margin. Tectonophysics 459, 66–84. http://dx.doi.org/10.1016/j.tecto.2007.11.067.

Vásquez, P., Glodny, J., Franz, G., Frei, D., Romer, R.L., 2011. Early Mesozoic plutonism of the Cordillera de la Costa (34°–37°S), Chile: constraints on the onset of the Andean Orogeny. J. Geol. 119, 159–184. http://dx.doi.org/10.1086/658296.

Völker, D., Grevemeyer, I., Stipp, M., Wang, K., He, J., 2011. Thermal control of the seismogenic zone of southern central Chile. J. Geophys. Res. 116, B10305. http://dx.doi.org/10.1029/2011JB008247.